De Gruyter Brill
Paradigm
ISSN 1335-8871

MEASUREMENT SCIENCE REVIEW

Journal homepage: https://reference-global.com/journal/MSR

Discretization of the Resistive Loading Profile for Dipole Antennas

Anatolii Kliuchka*, Rene Hartansky, Jozef Hallon, Jan Halgos, Jakub Krchnak

Department of Electrical Engineering, Faculty of Electrical Engineering and Information Technology, Slovak University of Technology, Ilkovicova, 3, 841 04 Bratislava, Slovakia, anatolii.kliuchka@stuba.sk, rene.hartansky@stuba.sk, jozef.hallon@stuba.sk, jan.halgos@stuba.sk, jakub.krchnak@stuba.sk

Abstract: This paper develops an integral-based methodology for converting the continuous Wu-King resistance-per-unit-length profile of dipole antennas into discrete lumped resistances. Each nonterminal resistance is obtained by integrating the prescribed profile over its represented interval, while the endpoint singularity is approximated by a finite terminal resistance. Performance is evaluated in receive mode using induced terminal voltage under plane-wave excitation as the principal metric. The main analysis considers an 80 mm dipole over 10 MHz-3.75 GHz with 2, 5, 10, and 15 resistive elements per arm. For 10 elements per arm, the peak-to-peak voltage variation over 10 MHz-2.5 GHz is 1.28 dB, compared with 0.69 dB for the continuous reference, while the upper 3 dB frequencies are 3.54 and 3.65 GHz, respectively. Increasing segmentation beyond 10 elements provides only modest improvement. The method is also evaluated for 40-120 mm dipoles and practical planar implementations. Planarization with the selected resistor parasitics produces moderate changes, whereas dielectric substrates cause substantially greater high-frequency degradation.

Keywords: broadband dipole antenna, resistive loading, distributed resistive profile, discretization methodology, frequency response

1. INTRODUCTION

The broadband performance of conventional dipole antennas is limited by end reflections, which produce standing-wave current distributions and a strongly frequency-dependent response. As a result, a conventional thin half-wave dipole has a relatively narrow bandwidth that depends on the conductor radius and the adopted matching criterion [1]. Resistive loading suppresses these reflections by progressively dissipating the current energy, thereby providing a smoother response over a wider frequency range. For example, Kanda et al. demonstrated that a 15 cm continuously tapered resistively loaded dipole maintained its receiving transfer function within ±3 dB from 200 MHz to beyond 3 GHz [2].

An ideal implementation requires a continuous impedance distribution along the antenna arms, which is challenging to manufacture because it demands accurate control of local resistivity, film thickness, or geometrical taper. The profile is therefore often approximated using discrete resistive elements. Existing approaches have determined lumped resistance values by evaluating the prescribed profile at segment midpoints or by multiplying the midpoint value by the corresponding segment length [3], [4]. The nonlinear variation of the Wu-King profile introduces some discrepancy when segment resistance is approximated by midpoint quadrature, particularly near the arm tip. The proposed methodology determines each nonterminal resistance from the analytical integral over its represented interval, while the terminal resistance is assigned separately.

The present work focuses on this discretization problem rather than on proposing a complete antenna solution. A resistively loaded dipole is used as a representative structure for developing and evaluating the proposed approach. As resistively loaded dipoles provide a suitable basis for broadband electric-field sensing, the methodology is evaluated in receive mode, with the antenna treated as an isolated sensing element under plane-wave excitation. The induced terminal voltage is used as the principal performance quantity to determine how accurately the discrete resistance distribution reproduces the broadband receiving response of the continuous reference profile. However, the underlying discretization procedure is not inherently restricted to electric-field probes or the particular dipole configurations investigated here, and may be applicable to other antenna geometries that use a prescribed continuous loading profile.

The proposed methodology is mainly evaluated over the frequency range from 10 MHz to 3.75 GHz. This range covers frequencies relevant to radiated-disturbance measurements in electromagnetic compatibility testing [5], several mobile-communication bands [6], and commonly

DOI: 10.2478/msr-2026-0039
*Corresponding author: anatolii.kliuchka@stuba.sk (A. Kliuchka)
© 2026 Institute of Measurement Science, SAS. This work is licensed under CC BY-NC-ND 4.0.

used industrial, scientific, medical, and short-range-device bands [7], [8]. It therefore overlaps with applications in electromagnetic interference measurements, radio spectrum monitoring, and RF field exposure assessment [9]. The selected frequency range covers a substantial change in the electrical size of the studied dipole, from electrically small behavior at low frequencies to a condition near 3.75 GHz, where the wavelength is approximately equal to the total dipole length.

The study examines segmentation density and geometrical scaling using dipole lengths from 40 to 120 mm. The 80 mm dipole with 10 resistive elements per arm is used as the principal configuration, while 2, 5, 10, and 15 resistive elements per arm are compared to assess segmentation effects. A practical planar model of the 80 mm dipole is also analyzed to evaluate the influence of resistor parasitics and dielectric substrates on the receiving response.

2. SUBJECT & METHODS

A theoretical formulation for continuously resistively loaded dipoles was developed by Wu and King [10]. The analysis begins with the integral equation for the electric field of a thin wire, derived from Maxwell's equations, and directly relates the axial magnetic vector potential to the longitudinal current distribution. For clarity and consistency, all variables are specified throughout the paper. In both the Wu-King formulation and the present study, the investigated dipole is aligned along the *z*-axis, such that $A(z)$, $I(z)$, and $Z'(z)$ denote the vector potential, current, and local loading impedance per unit length at position *z*, respectively. The length of a single arm is h, so that the total dipole length is $2h$. The central idea of the formulation [10] is that the dipole supports a traveling-wave type current distribution of the general form

$$I(z) \propto (h - |z|)e^{-jk|z|}, \tag{1}$$

where the amplitude decreases smoothly from the feed point toward the ends. The Wu-King approximation assumes that the dimensionless expansion coefficient Ψ, defined by the normalized ratio of the axial magnetic vector potential to the current, is approximately constant along the antenna arm:

$$\Psi(z) = \frac{4\pi}{\mu_0}\frac{A_z(z)}{I(z)} \approx \text{const.} \tag{2}$$

This implies that the electromagnetic self-interaction experienced by the current does not vary significantly along the conductor. Physically, this approximation corresponds to quasi-uniform propagation conditions along the dipole, allowing the structure to be viewed locally as a transmission line supporting a progressively damped forward-propagating wave. In a thin conductor, the relationship between the magnetic vector potential and the current depends only on the electrical length of the dipole and its geometric parameters. Consequently, for a given frequency and geometry, the proportionality coefficient Ψ is independent of the excitation amplitude.

A. Distributed resistive profile

In the Wu-King formulation, the traveling-wave current distribution in (1) is associated with a position-dependent loading impedance per unit length along the dipole arms. Based on [10]-[12], this impedance can be expressed as

$$Z'(z) = \frac{60\,\Psi}{h - |z|}. \tag{3}$$

The coefficient Ψ is determined by the electrical and geometrical parameters of the dipole. Under the thin-wire approximation, it is given by

$$\Psi = 2[\sin h^{-1}\left(\frac{h}{a}\right) - C(2A, 2kh) - jS(2A, 2kh)] + \\ + \frac{j}{kh}\left(1 - e^{-j2kh}\right), \tag{4}$$

where

$$A = ka, \qquad k = \frac{2\pi}{\lambda} = \frac{2\pi f}{c}.$$

Here, a is the conductor radius, $C(2A, 2kh)$ and $S(2A, 2kh)$ denote the generalized cosine and sine integrals used in the Wu-King formulation. The parameter ka represents the electrical radius of the conductor, while kh represents the electrical length of one dipole arm. The thin-wire assumption requires the conductor radius to be much smaller than both the arm length and the wavelength, i.e.

$$a \ll h, \qquad ka \ll 1.$$

The dipole arm length h influences both the achievable frequency range and receiving sensitivity. A shorter arm reduces the electrical length kh, shifting length-related resonant effects toward higher frequencies, but also decreases the effective receiving length and therefore the induced terminal voltage [13]. The selected arm length thus represents a compromise between bandwidth and sensitivity. Equation (4) generally yields a complex value of Ψ, containing both real and imaginary components. In the present resistive-loading analysis, only the real component is retained. Hereafter, Ψ denotes the retained real component of the coefficient. The resulting purely resistive profile approximates the complex Wu-King loading. Its receiving performance is therefore evaluated numerically, with the synthesized resistance values held fixed throughout each frequency sweep.

The value of Ψ depends on the dipole geometry and evaluation frequency and must therefore be recalculated when h, a, or f_{eval} changes. The principal configuration has a total length of $2h = 80$ mm, with $h = 40$ mm and $a = 0.125$ mm. The evaluation frequency was selected as 3.75 GHz so that the corresponding free-space wavelength, approximately 80 mm, equals the total physical length of the dipole. Substitution of the geometrical parameters and evaluation frequency of the principal configuration into (4) yields $\Psi = 8.0$ (rounded to one decimal place).

Using this value together with the parameters of the principal geometry in (3) yields the continuous resistance-per-unit-length distribution shown in Fig. 1. The resulting profile exhibits its minimum resistance near the feed point and increases monotonically toward the dipole ends, with the theoretical resistance tending to infinity at the arm tips.

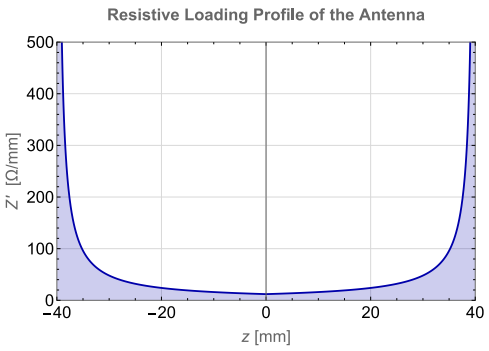

Fig. 1. Continuous resistive profile along the dipole arms.

Although the analytical formulation assumes an idealized thin cylindrical conductor with a continuous resistance distribution, the same loading principle can be applied to practical antenna geometries. In this study, the continuous profile serves as the common analytical basis for the continuous reference and the subsequent discrete approximation. For the subsequent full-wave analysis, the continuous reference is realized as a homogeneous resistive film with a triangular planar geometry. The width of each arm decreases linearly from its maximum value w_0 at the feed point to zero at the arm tip. The principal geometry retained an arm length of $h = 40$ mm, while the maximum film width was set to $w_0 = 1$ mm.

To relate the tapered strip geometry to the thin-wire formulation used in the evaluation of Ψ, an equivalent cylindrical radius was introduced. For the linear taper, the mean strip width is $w_{\text{avg}} = w_0/2 = 0.5$ mm. For an electrically narrow conducting strip, the equivalent cylindrical radius is given by $a_{\text{eq}} = w/4$ [14], a relation that has also been numerically assessed for strip dipoles with electrically small equivalent radii [15]. Applied to the mean width of the tapered arm, this relation gives $a_{\text{eq}} = 0.5/4 = 0.125$ mm, identical to the radius used in the preceding calculation of Ψ. This equivalent radius is an approximation used to evaluate Ψ and does not imply electromagnetic equivalence between the tapered resistive film and the cylindrical discrete model.

The previously obtained value $\Psi = 8.0$ is therefore retained for the triangular-film reference. The equivalent radius is used only for the analytical evaluation of Ψ, whereas the actual linearly tapered geometry is represented directly in the full-wave simulation.

For one dipole arm, extending over $0 \le z < h$, the linearly tapered width can be expressed as

$$w(z) = w_0\left(1 - \frac{z}{h}\right), \tag{5}$$

Assuming that the electrical resistivity ρ and film thickness t remain constant along the arm, the resistance per unit length of the film is

$$Z'(z) = \frac{\rho}{t\, w(z)}. \tag{6}$$

Substitution of the linear width distribution from (5) into (6) gives

$$Z'(z) = \frac{\rho}{t\, w_0\left(1 - \frac{z}{h}\right)} = \frac{\rho h}{t\, w_0 (h - z)}. \tag{7}$$

Equation (7) shows that the resistance per unit length produced by the triangular film satisfies

$$Z'(z) \propto \frac{1}{h - z}, \tag{8}$$

which is the same spatial dependence as the Wu-King profile defined in (3). Therefore, a linear decrease in the width of a film with constant resistivity and thickness produces the required hyperbolic increase in resistance per unit length toward the arm tip.

This principle has previously been applied in practical implementations. In resistively tapered electric-field probes, progressively reducing the strip width produced the required resistance variation and demonstrated broadband receiving behavior [16]. Kang and Kim applied a related approach using planar resistor technology, with the antenna-arm width selected according to the local Wu-King resistance profile. Simulated and measured time-domain responses showed no observable end reflections [17].

To determine the required sheet resistance for the triangular resistive film, (7) is equated to the positive-arm form of the Wu-King loading profile,

$$\frac{\rho h}{t\, w_0 (h - z)} = \frac{60\,\Psi}{h - z}. \tag{9}$$

After canceling the common spatial term $1/(h - z)$, the required sheet resistance becomes

$$R_s = \frac{\rho}{t} = w_0 \frac{60\,\Psi}{h}. \tag{10}$$

For the principal configuration, with $w_0 = 1$ mm, $h = 40$ mm, and $\Psi = 8$, the resulting sheet resistance is

$$R_s = 1\ \text{mm}\,\frac{60 \cdot 8}{40\ \text{mm}} = 12\ \Omega/\square. \tag{11}$$

Thus, for uniform resistivity and film thickness, the linear width taper analytically reproduces the $1/(h - z)$ dependence of the continuous Wu-King profile, providing the required continuous reference realization.

B. Integral-based discrete approximation

Continuous loading has been implemented using films with tapered thickness [2] or width [16], requiring control of material properties and geometry. Thick-film implementations introduce fabrication-dependent resistance tolerances [18], [19], while embedded planar resistor technology involves specialized materials and fabrication steps [17].

Discrete resistors provide an alternative compatible with conventional surface-mount assembly, and previous studies have demonstrated broadband operation using discrete loading [17], [20]. The following formulation determines the resistor values and positions from the prescribed continuous profile while accounting for the finite package length.

The discretization is formulated by preserving the resistance associated with each portion of the antenna arm. For each nonterminal interval, the assigned lumped resistance equals the integral of the prescribed resistance-per-unit-length profile over that interval. The singular terminal interval is treated separately using a finite resistance.

The discretization procedure is formulated below. Consider an antenna arm of length h, partitioned into N segments of length $\Delta z = h/N$, where the i-th segment extends from position $z_i = (i-1)\Delta z$ along the dipole axis to $z_i + \Delta z$, measured from the feed point. Within each segment, the continuously varying resistance per unit length is replaced by an equivalent lumped resistance R_i

$$R_i = \int_{z_i}^{z_i+\Delta z} Z'(z)\,\mathrm{d}z. \tag{12}$$

Substituting the expression for the internal impedance per unit length (3) into (12), the resistance of the i-th segment becomes

$$R_i = \int_{z_i}^{z_i+\Delta z} \frac{60\,\Psi}{h-|z|}\mathrm{d}z. \tag{13}$$

For a single dipole arm, where $z \geq 0$, the absolute value can be omitted, yielding

$$R_i = 60\,\Psi \int_{z_i}^{z_i+\Delta z} \frac{1}{h-z}\mathrm{d}z. \tag{14}$$

Evaluating the integral gives the analytical expression

$$R_i = 60\,\Psi \ln\left(\frac{h-z_i}{h-(z_i+\Delta z)}\right). \tag{15}$$

Equation (15) defines the equivalent resistance associated with each ideal equal-length segment of the continuous profile. Using this theoretical partition for the nonsingular segments and replacing the singular terminal value with the finite endpoint resistance yields the discrete profile of the principal geometry shown in Fig. 2.

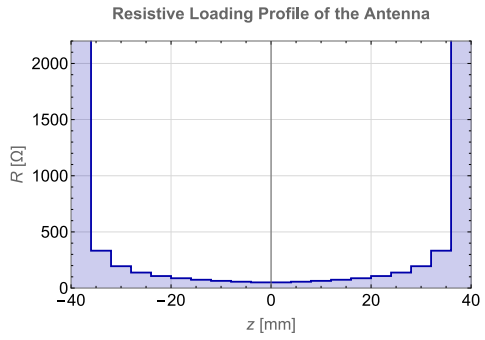

Fig. 2. Equal-segment approximation of the continuous resistive profile along the dipole arms.

For a practical realization, it is necessary to determine not only the segment boundaries but also the positions of the finite-size resistive elements so that each resistor represents the intended portion of the antenna arm. The following formulation, therefore, introduces the resistor package length r and determines both the element positions and the corresponding integration boundaries. In the proposed configuration, the leading edge of the first resistor package, i.e., the edge facing the feed point, coincides with the feed point, while the leading edge of each subsequent resistor defines the beginning of the corresponding represented segment. The center of each resistor is therefore located at a distance $r/2$ from the beginning of its corresponding segment. The final resistor package terminates at the arm tip, and the spacing between successive resistor centers is uniform. The final represented interval extends from the leading edge of the last resistor package to the arm tip. The center-to-center spacing is therefore defined as

$$\Delta l = \frac{h-r}{N-1}. \tag{16}$$

Once the spacing Δl is known, the center positions p_i of the resistors along the arm can be determined. The placement requires $N \geq 2$ and $\Delta l \geq r$ to prevent overlap between adjacent resistor packages.

Since the leading edge of the first resistor coincides with the feed point, its center position is

$$p_1 = \frac{r}{2}. \tag{17}$$

The general expression for the center position of the i-th resistor is

$$p_i = \frac{r}{2} + (i-1)\Delta l, \quad i = 1, 2, \ldots, N. \tag{18}$$

For the resistors $(i = 1, 2 \ldots, N-1)$, the represented segment boundaries are defined as

$$z_i^{(\mathrm{start})} = p_i - \frac{r}{2}, \tag{19}$$

$$z_i^{(\mathrm{end})} = p_i - \frac{r}{2} + \Delta l. \tag{20}$$

For the final resistor, the represented interval extends from the leading edge of the resistor package to the arm tip:

$$z_N^{(\mathrm{start})} = p_N - \frac{r}{2} = h - r \tag{21}$$

$$z_N^{(\mathrm{end})} = h \tag{22}$$

Substitution of (19) and (20) into (15) gives the resistance assigned to the i-th nonterminal element:

$$R_i = 60\,\Psi\,\ln\left(\frac{h-p_i+\frac{r}{2}}{h-p_i+\frac{r}{2}-\Delta l}\right), i = 1, 2 \ldots, N-1. \tag{23}$$

For the final element, extending the analytical integration to the arm tip yields a singular resistance. A finite endpoint resistance is therefore introduced for the numerical implementation, and its influence is evaluated separately in Section 3.*E*.

For the principal discrete configuration, the proposed segmentation methodology was applied using $N = 10$ resistive elements per arm. The element positions and nonterminal resistance values were calculated from (16)-(23), with the resistor package length set to $r = 1.6$ mm. The terminal resistance was set to 3 kΩ and the resulting values are listed in Table 1.

Table 1. Calculated positions and resistance values for the principal discrete dipole.

Resistor	Center Position p_i [mm]	Resistance R_i [Ω]
1	0.80	54.14
2	5.07	61.03
3	9.33	69.94
4	13.60	81.90
5	17.87	98.81
6	22.13	124.57
7	26.40	168.67
8	30.67	262.34
9	34.93	623.66
10	39.20	3000.00

The resulting discrete resistance distribution along the principal dipole is shown in Fig. 3.

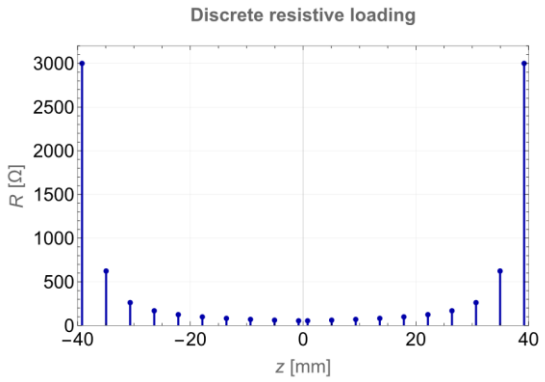

Fig. 3. Discrete resistive loading profile of the principal dipole.

C. Modeling and solver setup

Following the analytical formulation of the continuous and discrete loading profiles, both configurations were implemented in Altair FEKO for full-wave evaluation of the proposed discretization methodology. The continuous reference model used the triangular resistive-film realization derived in Section 2.*A*, with a sheet resistance of 12 Ω/□ for the principal configuration. The discrete model consisted of perfectly electrically conducting (PEC) dipole arms loaded with ten lumped resistive elements per arm, positioned according to the segmentation procedure described in Section 2.*B*. The two models are shown in Fig. 4.

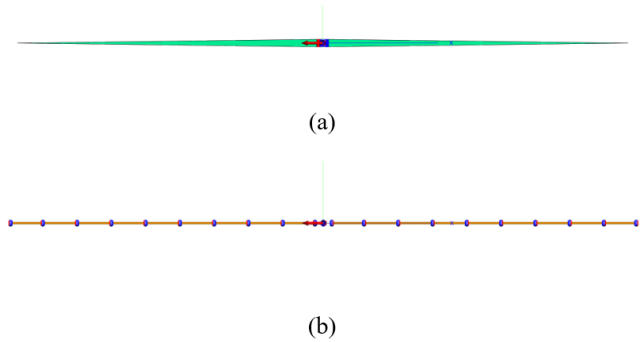

Fig. 4. Simulated antenna models: (a) continuous resistive loading; (b) discrete resistive loading.

In the baseline discrete model, the calculated resistances were represented as ideal, frequency-independent lumped elements. Component parasitics were excluded from the baseline models. The resulting comparison evaluates the agreement between the continuous-film and discrete thin-wire implementations and includes the influence of their different conductor representations. Parasitic inductance and capacitance are introduced separately in the practical planar models described in Section 2.*D*.

All simulations were performed using the frequency-domain method of moments. The continuous and discrete configurations were excited by the same uniform free-space plane wave with an electric-field strength of 1 V/m. The electric-field vector was aligned with the dipole axis to provide maximum coupling, while the direction of propagation was perpendicular to the antenna axis. The antenna models were placed in free space. The frequency response was calculated from 100 kHz to 10 GHz using 1001 linearly spaced frequency points with an increment of approximately 10 MHz. The dipole terminals were connected through a lumped high-impedance load of $Z_L = 1000$ MΩ to approximate open-circuit conditions and minimize receiver loading. Because the load impedance was much higher than the expected antenna terminal impedance, the load current was negligible, allowing differences in the simulated responses to reflect primarily the antenna loading implementation and its discretization. Unless otherwise specified, the same load impedance, excitation conditions, and solver settings were used for all continuous and discrete models. The modified frequency ranges and sampling used for the dielectric-supported and mesh-sensitivity models are described separately in the corresponding subsections.

The induced terminal voltage was reported in dBV according to

$$V_{\mathrm{dBV}}(f) = 20\log_{10}\left(\frac{|V(f)|}{1\ \mathrm{V}}\right) \tag{24}$$

The response flatness over a frequency interval $[f_1, f_2]$ was quantified as the peak-to-peak variation

$$F_{\mathrm{pp}} = \max_{f\in[f_1,f_2]} V_{\mathrm{dBV}}(f) - \min_{f\in[f_1,f_2]} V_{\mathrm{dBV}}(f). \tag{25}$$

To compare the discrete and continuous implementations, the signed voltage difference was defined as

$$\Delta V_{\mathrm{dB}}(f) = V_{\mathrm{cont,dBV}}(f) - V_{\mathrm{disc,dBV}}(f) = \\ = 20\log_{10}\left(\frac{|V_{\mathrm{cont}}(f)|}{|V_{\mathrm{disc}}(f)|}\right). \quad (26)$$

The maximum disagreement over a specified frequency interval was evaluated as

$$\Delta V_{\mathrm{dB,max}} = \max_f |\Delta V_{\mathrm{dB}}(f)|. \quad (27)$$

For each configuration, the reference level was calculated as the arithmetic mean of the terminal-voltage levels in dBV over 10-100 MHz. For the practical-model comparisons, the reference interval was 100-200 MHz. The upper 3 dB frequency was defined as the first downward crossing of a level 3 dB below the corresponding reference, with linear interpolation between adjacent frequency samples.

D. Planar and dielectric-supported models

To extend the idealized thin-wire analysis toward a more practical representation, the principal configuration was additionally modeled using 0.8 mm-wide planar strip conductors. The width was selected to accommodate the 0603 component layout. Using the strip-to-wire equivalence [14], the representative radius was $a_{\mathrm{eq}} = 0.2$ mm. The coefficient Ψ was recalculated for this geometry at $f_{\mathrm{eval}} = 3.75$ GHz, and the resistance values were subsequently recalculated using the discretization procedure described in (16)-(23). The adopted design coefficient for the planar geometry was $\Psi = 7.1$. For all planar models, each resistive element was represented by its nominal resistance in series with a parasitic inductance, with a parasitic capacitance connected across the complete R-L branch (RLC models). For the selected 0603 package, the values $L = 0.0267$ nH and $C = 0.0403$ pF were taken from the internal 0603 flip-chip model in [21] and applied to all nominal resistances. These values are most directly applicable to the nonterminal resistors within the 50-1000 Ω resistance range characterized in that source. The substrate-free planar comparison combines changes in conductor geometry, recalculation of the nominal resistance values, and the inclusion of the selected component parasitics. These factors collectively contribute to the observed change.

Three planar models were constructed: a substrate-free model in free space, a model on FR-4 with $\varepsilon_r = 4.4$, $\tan\delta = 0.02$, and thickness 0.6 mm, and a model on Rogers RT/duroid 5880 with $\varepsilon_r = 2.2$, $\tan\delta = 0.0009$, and thickness 0.508 mm (Fig. 5 below). The thin-wire model with ideal resistances was retained as the reference. Because low-frequency stabilization could not be enabled for the selected dielectric-supported MoM configurations, these models were evaluated from 0.10 to 10 GHz. Except for the stated frequency range, geometry, material properties, and resistor models, the excitation conditions, load impedance, and remaining solver settings were kept unchanged.

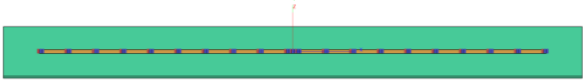

Fig. 5. Planar dipole model on a Rogers RT/duroid substrate.

E. Endpoint approximation and numerical sensitivity

The baseline simulations were generated using FEKO's automatic Fine mesh setting. The automatic meshing procedure determines the mesh size with consideration of the simulation frequency, solution method, dielectric properties, wavelength in the propagation medium, and geometrical curvature [22]. The custom refined mesh was used only for the mesh-sensitivity comparison.

The sensitivity to the finite approximation of the theoretical endpoint singularity was evaluated using the principal thin-wire model with 10 resistors per arm. Only the terminal resistance on each arm was varied from 1 to 300 kΩ, while all other model and solver parameters were kept unchanged. The 300 kΩ configuration was used as the reference.

To verify that the reported response was not significantly affected by mesh density, a mesh-sensitivity analysis was performed using the FR-4-supported planar model. This configuration was selected as a representative numerically demanding case because the dielectric reduces the wavelength within the substrate. FEKO recommends mesh-convergence verification using approximately 50 % more elements [23]. The automatic Fine mesh contained 5196 triangular elements, whereas the custom mesh contained 11640 elements, corresponding to a 124 % increase in element count. Both meshes were evaluated using 201 logarithmically spaced frequency points from 0.10 to 10 GHz, with all remaining model and solver parameters unchanged. The signed difference was defined as $\Delta V_{(\mathrm{mesh})}(f) = V_{\mathrm{Fine,dBV}}(f) - V_{\mathrm{Refined,dBV}}(f)$, with positive values corresponding to a higher induced terminal voltage obtained with the automatic Fine mesh.

3. RESULTS

A. Comparison of the principal continuous and discrete models

The proposed discretization methodology was first evaluated using the principal dipole configurations. The induced terminal voltage of the resulting discrete model with ten lumped resistive elements per arm was compared with that of the corresponding continuous triangular-film reference under identical plane-wave excitation and open-circuit-approximating load conditions. Fig. 6 presents the resulting voltage responses over the simulated frequency range. The intended evaluation range extends from 10 MHz to 3.75 GHz, while the response beyond this limit is shown only to illustrate the subsequent high-frequency roll-off.

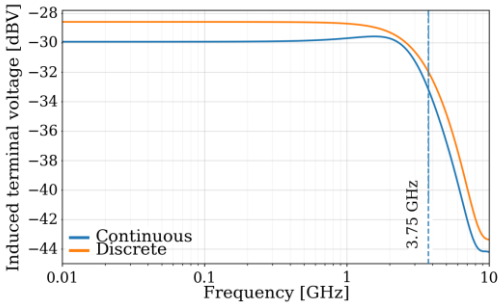

Fig. 6. Absolute induced terminal voltage of the continuous and discrete implementations of the 80 mm dipole.

Both configurations exhibit similar broadband frequency dependence, although the discrete model produces a systematically higher absolute terminal voltage. At 100 MHz, the continuous and discrete implementations yield −29.93 dBV and –28.58 dBV, respectively, while at 3.75 GHz, the corresponding values are –33.20 dBV and −32.00 dBV. This absolute sensitivity offset cannot be attributed solely to discretization, as the two models are derived from the same prescribed loading profile yet employ different conductor representations.

Since the primary objective is to assess how accurately the discrete loading reproduces the frequency-response shape of the continuous profile, response flatness and the upper 3 dB frequency are used as the main comparison metrics. Using the mean terminal voltage between 10 and 100 MHz as the reference level, the upper 3 dB frequencies are approximately 3.65 GHz and 3.54 GHz, respectively. Over the approximately flat region from 10 MHz to 2.5 GHz, the peak-to-peak variation defined in (25) is 0.69 dB for the continuous model and 1.28 dB for the discrete model. The continuous and discrete implementations exhibit comparable broadband response characteristics and upper 3 dB frequencies, despite the offset in absolute sensitivity.

To quantify the difference between the continuous-film and discrete thin-wire implementations, Fig. 7 presents the signed voltage difference $\Delta V_{\mathrm{dB}}(f)$ defined in (26). For the investigated models, $\Delta V_{\mathrm{dB}}(f)$ remains negative over the entire simulated frequency range, corresponding to a systematically higher terminal voltage in the discrete implementation.

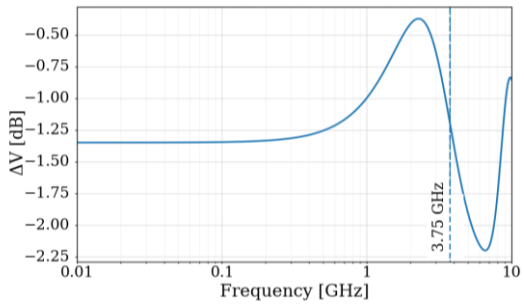

Fig. 7. Induced voltage difference between continuous and discrete implementations.

Within the intended 10 MHz-3.75 GHz evaluation range, the maximum absolute difference is 1.35 dB at the low-frequency end of the band, while the signed difference at $f_{\mathrm{eval}} = 3.75$ GHz is –1.20 dB.

B. Influence of segmentation density

Segmentation density was subsequently investigated for the 80 mm dipole using 2, 5, 10, and 15 resistive elements per arm. All configurations were compared with the continuous reference under identical excitation, loading, and solver conditions.

Fig. 8 shows that increasing the number of elements progressively improves agreement with the continuous broadband response. The two-resistor configuration deviates substantially at higher frequencies, indicating insufficient spatial resolution of the distributed loading. The 5-, 10-, and 15-resistor configurations preserve the general response shape, with the 10- and 15-resistor models closely overlapping over most of the investigated range.

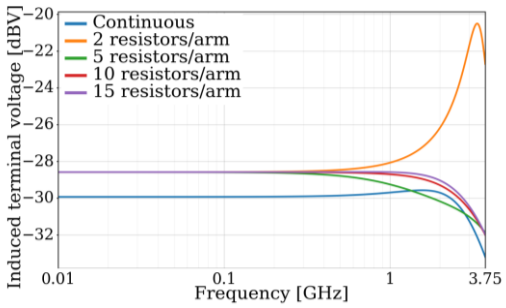

Fig. 8. Influence of segmentation density on the induced terminal voltage of the principal 80 mm dipole.

Since the 5-, 10-, and 15-resistor configurations exhibit similar upper 3 dB frequencies, segmentation density is more clearly distinguished by the peak-to-peak variation over the approximately flat 10 MHz-2.5 GHz interval. The continuous model yields 0.69 dB, compared with 4.27, 1.99, 1.28, and 1.05 dB for the 2-, 5-, 10-, and 15-resistor configurations, respectively (Fig. 9). The decreasing variation indicates improved reproduction of the continuous response with finer segmentation, with only modest improvement beyond 10 resistors per arm.

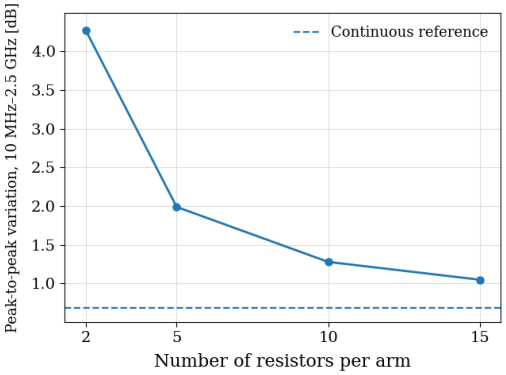

Fig. 9. Peak-to-peak variation of the induced terminal voltage in the 10 MHz-2.5 GHz interval as a function of the number of resistors per arm.

The upper 3 dB frequency was also evaluated relative to the mean terminal voltage in the 10-100 MHz interval. The continuous reference yielded 3.65 GHz, compared with 3.53, 3.54, and 3.58 GHz for the 5-, 10-, and 15-resistor configurations, respectively. The two-resistor configuration exhibits a pronounced voltage increase within the evaluation band; a single upper –3 dB crossing therefore does not adequately characterize its response flatness, further indicating insufficient segmentation.

Over the full 10 MHz-3.75 GHz evaluation range, the maximum absolute difference from the continuous reference was 11.73 dB for the 2-resistor configuration and approximately 1.35 dB for the remaining configurations (Fig. 10). In these cases, the maximum occurs at the low-frequency end and is strongly influenced by the previously

identified sensitivity offset. Flatness and upper 3 dB frequency, therefore, provide more representative measures of segmentation performance than the maximum absolute voltage difference alone.

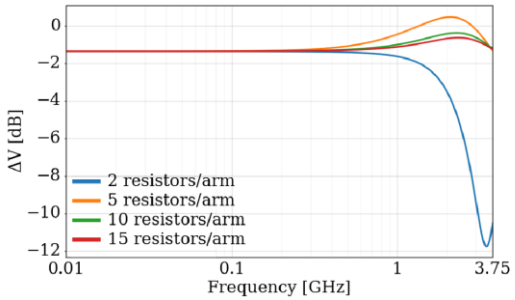

Fig. 10. Induced voltage difference between the continuous model and the discrete configurations of different segmentation densities.

Given the diminishing improvement at higher segmentation densities, the 10-resistor-per-arm configuration was retained as the principal discrete model for the subsequent analyses.

C. Geometrical scalability

Next, the geometrical scalability of the proposed method was evaluated. For total dipole lengths from 40 to 120 mm, five discrete configurations were evaluated against the corresponding continuous references. For each geometry, the evaluation frequency was selected to preserve the same normalized condition used for the principal configuration, in which the total dipole length equals the free-space wavelength,

$$\lambda_0 = 2h, \qquad f_{\mathrm{eval}} = \frac{c}{2h}.$$

Accordingly, f_{eval} ranged from 2.5 to 7.5 GHz. The Ψ coefficient was calculated for each geometry and its corresponding evaluation frequency using (4), and the resulting values are presented in Table 2.

Table 2. Dipole geometries and corresponding Wu-King parameters.

Total length $2h$ [mm]	Arm length h [mm]	Radius a [mm]	Evaluation frequency f [GHz]	Ψ
40	20	0.125	7.50	6.7
60	30	0.125	5.00	7.5
80	40	0.125	3.75	8.0
100	50	0.125	3.00	8.5
120	60	0.125	2.50	8.9

Using the geometry-specific parameters in Table 2, the sheet resistance of each continuous reference was calculated from (10), while the positions and resistance values of the corresponding ten-element discrete configurations were recalculated using (16)-(23).

Fig. 11 compares each discrete implementation with its continuous reference up to the corresponding f_{eval}, thereby maintaining the common normalized condition.

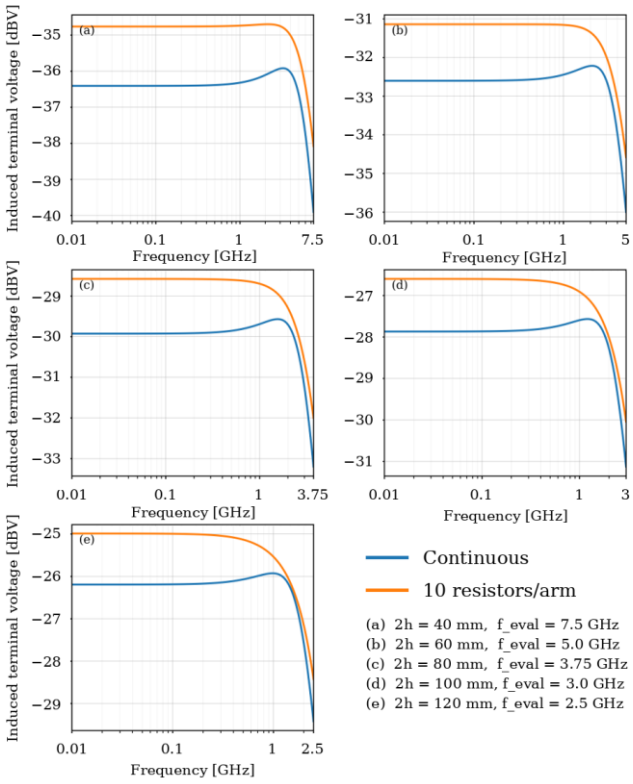

Fig. 11. Induced terminal voltage of the continuous and ten-resistor-per-arm implementations for total dipole lengths of (a) 40; (b) 60; (c) 80; (d) 100; and (e) 120 mm.

The discrete implementations reproduce the general frequency dependence of the continuous profiles for all investigated lengths. Increasing the dipole length increases the absolute received voltage while reducing the upper operating frequency, consistent with the expected trade-off between receiving sensitivity and high-frequency range.

Over 10 MHz $\leq f \leq f_{\mathrm{eval}}$, the peak-to-peak variation ranges from 3.49 to 3.98 dB for the continuous profiles and from 3.38 to 3.44 dB for the ten-resistor implementations. This interval includes the upper-frequency roll-off and differs from the 10 MHz-2.5 GHz interval used in the segmentation-density comparison.

The upper 3 dB frequency was determined relative to the mean terminal voltage between 10 and 100 MHz using the complete simulated frequency sweep. As shown in Fig. 12, it decreases with increasing dipole length and remains close to the geometry-specific reference $f_{\mathrm{eval}} = c/2h$. Across the investigated lengths, the continuous implementations yield 3 dB frequencies from 7.17 to 2.44 GHz, while the corresponding discrete models yield frequencies from 7.24 to 2.34 GHz.

Within the geometry-specific evaluation ranges, the maximum absolute difference between the continuous and discrete models decreases from 1.82 to 1.20 dB as the total dipole length increases from 40 to 120 mm. Although the discrete models exhibit a slightly higher absolute terminal voltage, preservation of the overall response shape and length-dependent upper-frequency trend indicates consistent performance of the discretization procedure across the investigated scaled geometries.

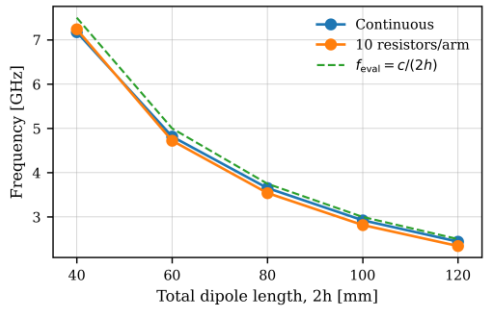

Fig. 12. Upper 3 dB frequency as a function of total dipole length for the continuous and 10-resistor-per-arm implementations.

D. Planar models and substrate effects

The influence of practical implementation effects was evaluated by comparing the ideal thin-wire reference with the substrate-free planar RLC (resistance with parasitics) model and the corresponding FR-4 and Rogers-supported configurations. Fig. 13 presents the absolute induced terminal voltages over the range of 0.1-10 GHz, with 3.75 GHz retained as the principal evaluation frequency.

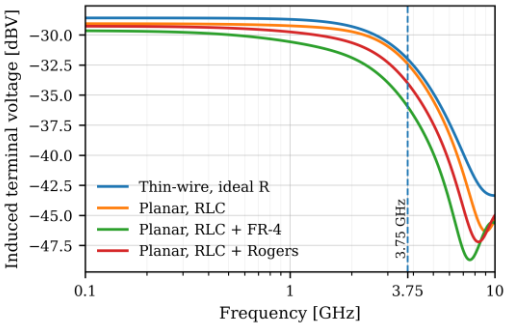

Fig. 13. Induced voltage of the thin-wire and planar dipole models.

Over 0.10-3.75 GHz, the maximum absolute voltage difference between the substrate-free planar model and the ideal thin-wire reference is 0.54 dB. This difference represents the combined effects of planar geometry, recalculated loading resistances, and the selected parasitic model.

The dielectric-supported configurations show a substantially larger effect. Relative to the substrate-free planar model, the FR-4 implementation introduces differences of approximately –0.59 dB at 0.1 GHz and −3.54 dB at 3.75 GHz, whereas the corresponding Rogers values are –0.21 and –1.60 dB. Both dielectric-supported models, therefore, exhibit lower induced terminal voltages than the substrate-free planar reference, with the investigated FR-4 configuration showing the stronger high-frequency reduction.

To complement the absolute-sensitivity comparison, the upper 3 dB frequency was evaluated relative to the mean terminal voltage over the 0.1-0.2 GHz range. It is 3.54 GHz for the thin-wire model and 3.59 GHz for the substrate-free planar model, but it decreases to approximately 2.43 GHz with FR-4 and 3.00 GHz with Rogers. The signed voltage difference between the substrate-free planar and thin-wire models (Fig. 14) is small and nearly frequency-independent over the principal range. Relative to the substrate-free planar model, the substrate-supported models exhibit frequency-dependent voltage reductions, stronger for FR-4 than for Rogers (Fig. 15). These results indicate that dielectric loading has the dominant influence on the high-frequency response among the investigated implementation effects.

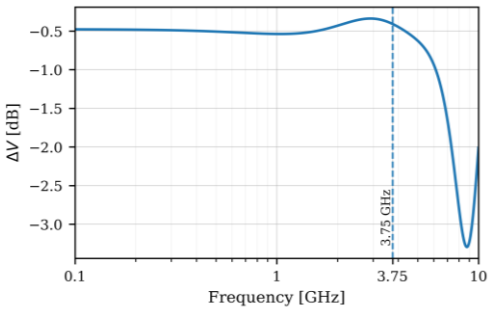

Fig. 14. Signed terminal-voltage difference between the substrate-free planar RLC model and the ideal thin-wire reference.

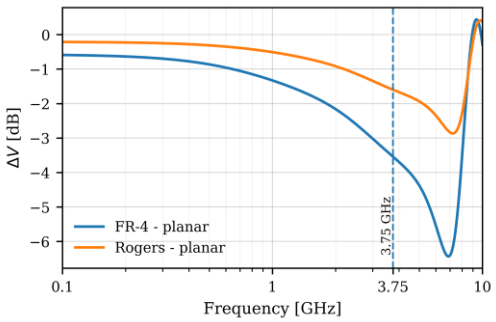

Fig. 15. Signed terminal-voltage difference relative to the substrate-free planar RLC model.

E. Endpoint-resistance truncation and mesh sensitivity

Endpoint-resistance truncation

For the endpoint-resistance sweep described in Section 2.*E*, the induced-voltage responses remained closely aligned throughout the intended frequency range. For the selected terminal resistance of 3 kΩ, the difference from the reference at 3.75 GHz was only –0.027 dB. The results summarized in Table 3 indicate only weak dependence of the receiving response on the finite endpoint resistance, while a value of 3 kΩ provides an adequate truncation for the investigated geometry and frequency range.

Table 3. Sensitivity of the receiving response to the endpoint resistance.

R_{tip} [kΩ]	Maximum absolute difference from 300 kΩ [dB]	Difference at 3.75 GHz [dB]	f_{3dB} [GHz]
1	0.110	–0.039	3.535
3	0.109	–0.027	3.541
10	0.105	–0.005	3.554
30	0.092	0.001	3.559
100	0.057	0.0004	3.564
300	Reference	-	3.579

Mesh sensitivity

For the FR-4-supported model, the two meshes described in Section 2.*E* yielded closely aligned induced-voltage responses. Over 0.10-3.75 GHz, the maximum absolute difference was only 0.0195 dB, increasing to 0.0542 dB over the complete 0.10-10 GHz range (Fig. 16).

Using the 0.10-0.20 GHz reference interval and the procedure defined in Section 2.*E*, the estimated upper 3 dB frequencies were 2.429 GHz for the automatic Fine mesh and 2.424 GHz for the refined mesh, corresponding to a difference of approximately 0.20 %. For the FR-4-supported model, the investigated mesh refinement had only a minor effect on the terminal-voltage response and the estimated upper 3 dB frequency.

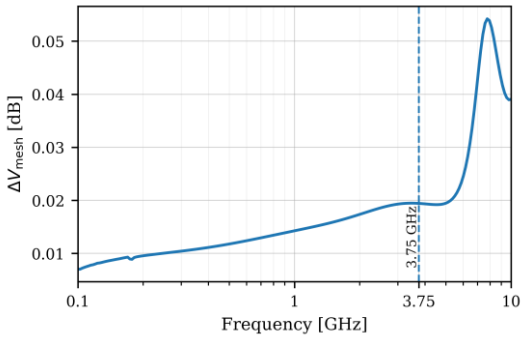

Fig. 16. Mesh-sensitivity comparison for the FR-4 model.

4. Discussion

The observed response trends can be interpreted in terms of the underlying resistive-loading mechanism, the spatial discretization of the profile, geometrical scaling, and practical implementation effects.

The integral assignment preserves the total resistance of each nonterminal interval, while its electromagnetic representation remains approximate because the distributed loading is concentrated at discrete positions. For fixed h, r, and Ψ, the nonterminal resistances sum to $60\,\Psi\ln(h/r)$, independently of the number of elements. Increasing segmentation density therefore redistributes a fixed total resistance over more positions and shortens the intervals represented by individual loads. The observed improvement in voltage flatness is consistent with this finer spatial representation. The remaining absolute voltage offset may also reflect differences between the continuous-film and discrete thin-wire geometries.

The scaling analysis concerns the transferability of the discretization procedure, not the direct scaling of a fixed resistor set. Under the adopted condition $2h = \lambda_0$, the normalized arm length kh is preserved at the geometry-specific evaluation frequency. The conductor radius a remains fixed, however, so the electrical radius ka changes as the dipole length changes. Since Ψ depends on both kh and ka, its value also varies between the investigated geometries. Although Ψ also varies with frequency through kh and ka, a physical resistive distribution is fixed after model realization. The study evaluates length variation with recalculated loading while retaining fixed resistor package length and transverse dimensions. Their ratios to the arm length therefore vary, so the investigated configurations do not represent uniform geometric scaling.

The practical-model comparisons address implementation effects that are not captured by the idealized thin-wire model. Substrates alter the effective wavelength and current distribution, changing the electromagnetic conditions for a profile derived in free space. The method converts a prescribed continuous resistance distribution into lumped values but does not compensate for these environmental changes. The stronger effect observed for FR-4 cannot be attributed to a single parameter, as the compared substrates differ in permittivity, dielectric loss, and thickness.

These findings are limited to receive-mode simulations with a load approximating an open circuit, minimizing receiver interaction to isolate antenna and discretization behavior. Future work will prioritize a high-input-impedance low-noise amplifier that preserves the broadband response for electric-field sensing, followed by implementation and experimental validation of the complete sensing structure.

5. Conclusion

An integral-based procedure was developed to convert the continuous Wu-King resistance-per-unit-length profile into discrete lumped resistances while accounting for finite component length. Nonterminal values preserve the resistance of their represented intervals, and the endpoint singularity is approximated by a finite terminal resistance.

Receive-mode full-wave simulations demonstrated close agreement in voltage-response flatness and upper 3 dB frequency for the principal configuration. Increasing segmentation provided diminishing improvement, and comparisons across different dipole lengths supported the application of the procedure with recalculated loading parameters. The practical-model comparisons showed that the selected dielectric supports substantially modified the high-frequency response, indicating that substrate effects should be accounted for in antenna design.

These findings were obtained for isolated dipoles under plane-wave excitation with a terminal load approximating an open circuit. Experimental validation and characterization of the receiving interface are priorities for future work.

Appendix

The Appendix provides the calculated loading parameters and element positions for configurations not fully tabulated in the main text. Table 4 summarizes the parameters of the continuous configurations. Table 5-Table 8 list the calculated resistor positions and resistance values for the 40, 60, 100, and 120 mm dipoles, respectively, with ten resistors per arm. Table 9-Table 11 provide the corresponding values for the 80 mm dipole with two, five, and fifteen resistors per arm, respectively. Table 12 presents the values for the 80 mm planar model. Owing to dipole symmetry, only one arm is tabulated. The Ψ values listed in Table 2 were adopted as design constants. The tabulated results are rounded for presentation.

Table 4. Parameters of the continuous configurations.

$2h$ [mm]	R_s [Ω/□]	Evaluation frequency f [GHz]	Ψ
40	20.10	7.50	6.7
60	15.00	5.00	7.5
80	12.00	3.75	8.0
100	10.20	3.00	8.5
120	8.90	2.50	8.9

Table 5. Calculated positions and resistance values for the 40 mm dipole with ten resistors per arm.

Resistor	Center position p_i [mm]	Resistance R_i [Ω]
1	0.80	43.34
2	2.84	48.59
3	4.88	55.28
4	6.93	64.12
5	8.97	76.32
6	11.02	94.29
7	13.06	123.42
8	15.11	179.01
9	17.15	330.92
10	19.20	3000.00

Table 6. Calculated positions and resistance values for the 60 mm dipole with ten resistors per arm.

Resistor	Center position p_i [mm]	Resistance R_i [Ω]
1	0.80	50.01
2	3.95	56.27
3	7.11	64.33
4	10.26	75.08
5	13.42	90.17
6	16.57	112.89
7	19.73	151.05
8	22.88	229.02
9	26.04	490.18
10	29.20	3000.00

Table 7. Calculated positions and resistance values for the 100 mm dipole with ten resistors per arm.

Resistor	Center position p_i [mm]	Resistance R_i [Ω]
1	0.80	58.03
2	6.17	65.49
3	11.55	75.16
4	16.93	88.18
5	22.31	106.69
6	27.68	135.08
7	33.06	184.28
8	38.44	291.40
9	43.82	751.09
10	49.20	3000.00

Table 8. Calculated positions and resistance values for the 120 mm dipole with ten resistors per arm.

Resistor	Center position p_i [mm]	Resistance R_i [Ω]
1	0.80	61.11
2	7.28	69.02
3	13.77	79.29
4	20.26	93.16
5	26.75	112.92
6	33.24	143.38
7	39.73	196.61
8	46.22	314.52
9	52.71	865.34
10	59.20	3000.00

Table 9. Calculated positions and resistance values for the 80 mm dipole with two resistors per arm.

Resistor	Center position p_i [mm]	Resistance R_i [Ω]
1	0.80	1545.06
2	39.20	3000.00

Table 10. Calculated positions and resistance values for the 80 mm dipole with five resistors per arm.

Resistor	Center position p_i [mm]	Resistance R_i [Ω]
1	0.80	131.72
2	10.40	182.15
3	20.00	297.13
4	29.60	934.03
5	39.20	3000.00

Table 11. Calculated positions and resistance values for the 80 mm dipole with fifteen resistors per arm.

Resistor	Center position p_i [mm]	Resistance R_i [Ω]
1	0.80	34.09
2	3.54	36.70
3	6.28	39.74
4	9.02	43.33
5	11.77	47.64
6	14.51	52.89
7	17.25	59.45
8	20.00	67.87
9	22.74	79.08
10	25.48	94.73
11	28.22	118.14
12	30.97	157.06
13	33.71	234.98
14	36.45	479.29
15	39.20	3000.00

Table 12. Calculated positions and resistance values for the 80 mm dipole planar model.

Resistor	Center position p_i [mm]	Resistance R_i [Ω]
1	0.80	48.05
2	5.06	54.16
3	9.33	62.07
4	13.60	72.68
5	17.86	87.69
6	22.13	110.55
7	26.40	149.69
8	30.66	232.82
9	34.93	553.49
10	39.20	3000.00

The FR-4 and Rogers RT/duroid 5880 substrates used in the planar models had lateral dimensions of 10 × 90 mm, with thicknesses of 0.6 mm and 0.508 mm, respectively.

Acknowledgment

Funded by the EU NextGenerationEU through the Recovery and Resilience Plan for Slovakia under the project 09I05-03-V02-00041.

References

[1] Estarki, M. D., Vaughan, R. G. (2013). Theoretical methods for the impedance and bandwidth of the thin dipole. *IEEE Antennas and Propagation Magazine*, 55 (1), 62-81. https://doi.org/10.1109/MAP.2013.6474485

[2] Kanda, M., Ries, F. X., Belsher, D. R. (1979). *A broadband, isotropic, real-time electric-field sensor (BIRES) using resistively loaded dipoles*. Technical Report NBS IR 79-1622. https://doi.org/10.6028/NBS.IR.79-1622

[3] Lu, W., Li, Y., Ji, Y., Shen, S., Tang, C., Zhou, B., Fang, G. (2021). High reliability UWB monopole antenna using planar embedded resistance for Mars subsurface exploration. *Electronics*, 10 (6), 682. https://doi.org/10.3390/electronics10060682

[4] Formato, R. (2011). New techniques for increasing antenna bandwidth with impedance loading. *Progress In Electromagnetics Research B*, 29, 269-288. https://doi.org/10.2528/PIERB11021904

[5] IEC. (2019). *Specification for radio disturbance and immunity measuring apparatus and methods - Part 2-3: Methods of measurement of disturbances and immunity - Radiated disturbance measurements*. Standard CISPR 16-2-3:2016+AMD1:2019. https://webstore.iec.ch/en/publication/65357

[6] ETSI. (2016). *IMT cellular networks; Harmonised Standard covering the essential requirements of Article 3.2 of Directive 2014/53/EU; Part 11: CDMA Direct Spread (UTRA FDD) Repeaters*. Standard ETSI EN 301 908-11 V11.1.1. https://www.etsi.org/deliver/etsi_en/301900_301999/30190811/11.01.01_60/en_30190811v110101p.pdf

[7] ITU. (2010). *Impact of industrial, scientific and medical (ISM) equipment on radiocommunication services*. Technical Report ITU-R SM.2180. https://www.itu.int/pub/R-REP-SM.2180

[8] ECPTA. (2026). *Relating to the use of Short Range Devices (SRD)*. ERC Recommendation 70-03. https://docdb.cept.org/document/845

[9] IEC. (2025). *Determination of RF field strength, power density and SAR in the vicinity of base stations for the purpose of evaluating human exposure.* Standard IEC 62232:2025. https://webstore.iec.ch/en/publication/89073

[10] Wu, T., King, R. (1965). The cylindrical antenna with nonreflecting resistive loading. *IEEE Transactions on Antennas and Propagation*, 13 (3), 369-373. https://doi.org/10.1109/TAP.1965.1138429

[11] Kanda, M. (1977). *A relatively short cylindrical broadband antenna with tapered resistive loading for picosecond pulse measurements*. NBS Internal Report NBSIR 77-861. https://doi.org/10.6028/NBS.IR.77-861

[12] Harťanský, R., Hallon, J. (2016). *Senzory pre meranie elektromagnetického poľa [Sensors for measurement of the electromagnetic field]*. Bratislava, Slovakia: Slovak University of Technology, ISBN 978-80-227-4565-9.

[13] Balanis, C. A. (2016). *Antenna Theory: Analysis and design, 4th Edition*. John Wiley & Sons, ISBN 978-1-118-64206-1.

[14] Butler, C. M. (1982). The equivalent radius of a narrow conducting strip. *IEEE Transactions on Antennas and Propagation*, 30 (4), 755-758. https://doi.org/10.1109/TAP.1982.1142839

[15] Keyrouz, S., Visser, H. J., Tijhuis, A. G. (2013). Novel empirical equations to calculate the impedance of a strip dipole antenna. *Radioengineering*, 22 (4), 1258-1261. https://www.radioeng.cz/fulltexts/2013/13_04_1258_1261.pdf

[16] Randa, J., Kanda, M., Melquist, D. (1988). *Possible designs for electric-field-strength probes for millimeter waves*. Technical Report NBSIR 88-3084. https://nvlpubs.nist.gov/nistpubs/Legacy/IR/nbsir88-3084.pdf

[17] Kang, W., Kim, K. (2018). Design and fabrication of resistively loaded dipoles using planar resistor technology. In *2018 International Symposium on Antennas and Propagation (ISAP)*. IEEE, 249-250. https://ieeexplore.ieee.org/document/8627811

[18] Hlina, J., Reboun, J., Johan, J., Simonovsky, M., Hamacek, A. (2019). Reliability of printed power resistor with thick-film copper terminals. *Microelectronic Engineering*, 216, 111095. https://doi.org/10.1016/j.mee.2019.111095

[19] Dziedzic, A., Kolek, A., Ehrhardt, W., Thust, H. (2006). Advanced electrical and stability characterization of untrimmed and variously trimmed thick-film and LTCC resistors. *Microelectronics Reliability*, 46 (2-4), 352-359. https://doi.org/10.1016/j.microrel.2004.12.014

[20] Kim, K., Scott Jr., W. R. (2004). Design and realization of a discretely loaded resistive vee dipole for ground-penetrating radars. *Radio Science*, 39 (4). https://doi.org/10.1029/2003RS002947

[21] Vishay Intertechnology, Inc. (2009). *Frequency response of thin film chip resistors*. Technical Note 60107. https://www.vishay.com/docs/60107/freqresp.pdf

[22] Altair Engineering, Inc. (2026). *Auto determine the mesh sizes*. Altair Feko Documentation. https://help.altair.com/feko/topics/feko/user_guide/cadfeko/mesh_automatic_feko_c-cadfeko.htm

[23] Altair Engineering, Inc. (2026). *Mesh overview*. Altair Feko Documentation. https://help.altair.com/feko/topics/feko/user_guide/cadfeko/mesh_overview_feko_c-cadfeko.htm

Received April 17, 2026
Accepted September 24, 2026